Spatial Resolution Limit of Ghost Imaging Camera via Sparsity Constraints –break Rayleigh's criterion based on the discernibility in high-dimensional light field space

Zhishen Tong,[1,2,*] Zhentao Liu,[1,*] Jian Wang,[3] Xia Shen[1] and Shensheng Han[1,4†]
[1] *Shanghai Institute of Optics and Fine Mechanics, Chinese Academy of Sciences, China*
[2] *Center of Materials Science and Optoelectronics Engineering, University of Chinese Academy of Sciences, Beijing, China*
[3] *School of Data Science, Fudan University, China*
[4] *Hangzhou Institute for Advanced Study, University of Chinese Academy of Sciences, Hangzhou, China*

By encoding high-dimensional light filed imaging information into a detectable two-dimensional plane, ghost imaging camera via sparsity constraints (GISC camera) can directly catch the high-dimensional light filed imaging information in a snapshot. This makes it worth to revisit the limitation of spatial resolution of these optical imaging systems. Here we show both theoretically and experimentally that, though the resolution in high-dimensional light filed space is still limited by diffraction, the spatial resolution of GISC camera can be greatly improved comparing to Rayleigh's criterion by increasing the discernibility in other dimensions of the high-dimensional light field space. Our results demonstrate that far-field super-resolution is achievable by utilizing the imaging channel capability of an incoherent imaging system more efficiently.

Due to the diffraction of light, Rayleigh's criterion has been the most influential resolution limit of incoherent optical imaging system for over a century [1]. In recent decades, various exciting optical techniques aiming at breaking Rayleigh's criterion have emerged. By utilizing structured illumination with several sinusoidal striped patterns or restricting the focused light spot with pinholes, one can break the diffraction limit of the corresponding imaging system, represented by the structured illumination microscopy (SIM) [2] and confocal laser scanning microscopy (CLSM) [3], despite the fact that they are still limited by diffraction including illumination system. While for scanning imaging systems, reducing the size of scanning point based on near-field or stimulated emission depletion effect, represented by the near-field scanning optical microscopy (NSOM) [4] and stimulated emission depletion microscopy (STED) [5], also render Rayleighs criterion irrelevant to the imaging resolution. Another category for far-field super-resolution technology is based on statistical methods [6, 7] reprensented by stochastic optical reconstruction microscopy (STORM) [6] and photoactivated localization microscopy (PALM) [7], where the positions of fluorescence molecules are accurately estimated and then a global picture as a whole is formed. More recently, a variety of both classical and non-classical quantum effects are also investigated to overcome Rayleighs curse [8–10]. In parallel to above physical super-resolution technologies, plenty of super-resolution algorithms [11] are developed to create the super-resolution image from low-resolution images, such as the spectrum extrapolation [12], multi-frame super-resolution [13], and deep learning [14].

Light field can be fully characterized by a high-dimensional plenoptic function [15]. By now, nearly all imaging systems is based on a point-to-point imaging mode, where the emission light from each point in real space (or spacial Fourier space) on the object plane is directly recorded by the corresponding pixel on the imaging plane of the system. This kind of imaging mode makes directly imaging in high-dimensional light filed space in a snapshot very difficult, and the corresponding super-resolution imaging techniques to improve the spatial resolving power of conventional imaging system are equivalent to increasing the precision of separating two adjacent point light sources on object plane of real space. Different from conventional imaging schemes, ghost imaging (GI) extracts objects information from the mutual correlation of light intensity fluctuation[16]. By encoding high-dimensional information of light field irradiated from the object plane into speckle patterns on a detectable two-dimensional plane, ghost imaging camera via sparsity constraints (GISC camera) [17] can directly record object's high-dimensional information in a snapshot. Besides directly increasing the accuracy of determining the positions of two adjacent point sources on the object plane of imaging system, GISC camera provides a new kind of possibility to break Rayleighs criterion via the discernibility in the high-dimensional (e.g., spatial dimension, spectrum, polarization) light field space.

In this paper, we firstly introduce GISC camera's schematic diagram, and analyze its resolution in high-dimensional light field space. Then, simulated and experimental results, which demonstrate the super-resolution capacity of GISC camera, are presented. Finally, we give the discussion and conclusion.

The schematic of GISC camera is shown in Fig. 1. The object is projected onto the focus plane through a conventional optical imaging system, which is composed of the objective lens with focus length f_1 and aperture D, and the tube lens with focus length f_2 after the objective lens with distance L. The light field after the focus plane with distance z_1 is modulated by a spatial random phase

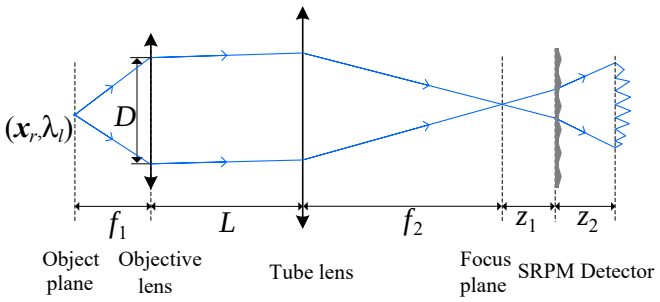

FIG. 1. The schematic of GISC camera.

modulator (SRPM), and the light intensity distribution behind SRPM with distance z_2 is detected by a detector.

Considering the incoherent illumination, the speckle intensity on the detection plane of GISC camera is [17]

$$I_t(\mathbf{x}_t) = \iint T(\mathbf{x}_r,\lambda_l) I_r(\mathbf{x}_t;\mathbf{x}_r,\lambda_l) d\mathbf{x}_r d\lambda_l, \tag{1}$$

where $T(\mathbf{x}_r,\lambda_l)$ represents high-dimensional $(\mathbf{x}_r,\lambda_l)$ image of object, $I_r(\mathbf{x}_t;\mathbf{x}_r,\lambda_l)$, which is detected in the predetermined process, denotes the system response of GISC camera corresponding to one monochrome point light source with wavelength λ_l at the position $\mathbf{x}_r$. $\mathbf{x}_r$ and $\mathbf{x}_t$ are two-dimensional vectors on the object plane and the detection plane of GISC camera, respectively.

From the viewpoint of GI [17, 18], each pixel of CCD detector acts as a bucket detector of the test arm, and $I_r(\mathbf{x}_t;\mathbf{x}_r,\lambda_l)$ for the fixed x_t acts as a pixelated signal of the reference arm. The high-dimensional image of object is recovered by calculating the second-order correlation function between the intensity fluctuations at the predetermined reference arm and test arm [17],

$$\begin{aligned}\Delta G^{(2,2)}(\mathbf{x}_r,\lambda_l) &= \langle \Delta I_t(\mathbf{x}_t)\Delta I_r(\mathbf{x}_t;\mathbf{x}_r,\lambda_l)\rangle_{\mathbf{x}_t} \\ &\overset{(1)}{=} \iint T(\mathbf{x}'_r,\lambda'_l)\Delta G_r^{(2,2)}(\mathbf{x}_r,\lambda_l;\mathbf{x}'_r,\lambda'_l) d\mathbf{x}'_r d\lambda'_l,\end{aligned} \tag{2}$$

where $\langle\cdots\rangle_{\mathbf{x}_t}$ means the spatial average over the coordinate $\mathbf{x}_t$, (for simplicity, the subscript $\mathbf{x}_t$ is omitted in the following content), and

$$\Delta I_t(\mathbf{x}_t) = I_t(\mathbf{x}_t) - \langle I_t(\mathbf{x}_t)\rangle, \tag{3a}$$

$$\Delta I_r(\mathbf{x}_t;\mathbf{x}_r,\lambda_l) = I_r(\mathbf{x}_t;\mathbf{x}_r,\lambda_l) - \langle I_r(\mathbf{x}_t;\mathbf{x}_r,\lambda_l)\rangle, \tag{3b}$$

$$\Delta G_r^{(2,2)}(\mathbf{x}_r,\lambda_l;\mathbf{x}'_r,\lambda'_l) = \langle \Delta I_r(\mathbf{x}_t;\mathbf{x}_r,\lambda_l)\Delta I_r(\mathbf{x}_t;\mathbf{x}'_r,\lambda'_l)\rangle \ . \tag{3c}$$

Equation (2) implies that the physical resolution of GISC camera is determined by $\Delta G_r^{(2,2)}(\mathbf{x}_r,\lambda_l;\mathbf{x}'_r,\lambda'_l)$. In many cases, the light field $E_r(\mathbf{x}_t;\mathbf{x}_r,\lambda_l)$ of the predetermined reference speckle pattern obeys the complex circular Gaussian distribution [19]. By the moment theorem for complex Gaussian process [20], we have

$$\Delta G_r^{(2,2)}(\mathbf{x}_r,\lambda_l;\mathbf{x}'_r,\lambda'_l) = |\langle E_r^*(\mathbf{x}_t;\mathbf{x}_r,\lambda_l) E_r(\mathbf{x}_t;\mathbf{x}'_r,\lambda'_l)\rangle|^2, \tag{4}$$

and the normalized second-order correlation function is

$$\begin{aligned} g^{(2)}(\mathbf{x}_r,\mathbf{x}'_r;\lambda_l,\lambda'_l) &\overset{def}{=} \frac{\Delta G_r^{(2,2)}(\mathbf{x}_r,\lambda_l;\mathbf{x}'_r,\lambda'_l)}{\langle I(\mathbf{x}_t;\mathbf{x}_r,\lambda_l)\rangle\langle I(\mathbf{x}_t;\mathbf{x}'_r,\lambda'_l)\rangle} \\ &\overset{(4)}{=} \frac{|\langle E_r^*(\mathbf{x}_t;\mathbf{x}_r,\lambda_l) E_r(\mathbf{x}_t;\mathbf{x}'_r,\lambda'_l)\rangle|^2}{\langle I(\mathbf{x}_t;\mathbf{x}_r,\lambda_l)\rangle\langle I(\mathbf{x}_t;\mathbf{x}'_r,\lambda'_l)\rangle}. \end{aligned} \tag{5}$$

According to the Fresnel diffraction theorem, the light field $E(\mathbf{x}_t;\mathbf{x}_r,\lambda_l)$ on the detector plane is

$$\begin{aligned} E_r(\mathbf{x}_t;\mathbf{x}_r,\lambda_l) = {} & \frac{E_0 D^2}{4\lambda_l^4 z_1 z_2 f_2 L} \exp\left(\frac{j\pi(2f_1^2+1)\mathbf{x}_r^2}{\lambda_l f_1}\right) \iint \exp\left(\frac{j\pi}{\lambda_l}\left(\frac{t}{f_2}+\frac{1}{z_1}\right)\mathbf{x}_1^2\right) \frac{J_1\left(2\pi\frac{D}{2\lambda_l f_2}\left(\frac{f_2}{f_1}\mathbf{x}_r+\mathbf{x}_1\right)\right)}{\frac{D}{2\lambda_l f_2}\left(\frac{f_2}{f_1}\mathbf{x}_r+\mathbf{x}_1\right)} \\ & \times \exp\left(\frac{-2j\pi}{\lambda_l z_1}\mathbf{x}_1\mathbf{x}_2\right) \exp\left(\frac{j\pi}{\lambda_l z_1}\mathbf{x}_2^2\right) \exp\left(\frac{j\pi}{\lambda_l z_2}(\mathbf{x}_t-\mathbf{x}_2)^2\right) t_h(\mathbf{x}_2,\lambda_l) d\mathbf{x}_1 d\mathbf{x}_2, \end{aligned} \tag{6}$$

where E_0 denotes the amplitude of light field of the monochromatic point light source, $\mathbf{x}_1$ and $\mathbf{x}_2$ are two-dimensional vectors on the focus plane and the front plane of SRPM, respectively. $J_1(\cdot)$ is the 1st-order Bessel function, $t := 1-L/f_2$ and $t_h(\mathbf{x}_2,\lambda_l)$ is the transmittance function of SRPM. The autocorrelation function of the height $\eta(\mathbf{x})$ of SRPM is assumed as [21]

$$R_\eta(\mathbf{x},\mathbf{x}') = \langle \eta(\mathbf{x})\eta(\mathbf{x}')\rangle = \omega^2 e^{-(\mathbf{x}-\mathbf{x}')^2/\zeta^2}, \tag{7}$$

where ω and ζ are the standard deviation and the lateral correlation length of the height of SRPM, respectively.

Substituting Eq. (6) into Eq. (5) yields

$$\begin{aligned} & g^{(2)}(\mathbf{x}_r,\mathbf{x}'_r;\lambda_l,\lambda'_l) \\ & \quad = \exp\left\{-\left(\frac{2\pi(n-1)\omega\Delta\lambda}{\overline{\lambda}^2}\right)^2\right\}\left(\frac{2J_1(\frac{\pi D\Delta\mathbf{x}}{\overline{\lambda} f_1})}{\frac{\pi D\Delta\mathbf{x}}{\overline{\lambda} f_1}}\right)^2, \end{aligned} \tag{8}$$

with the condition

$$\frac{\zeta|z_1+z_2|}{\omega|z_2|} \ll 2\pi(n-1)\frac{f}{D}, \tag{9}$$

where $\Delta\lambda = \lambda_l - \lambda'_l$, and $\Delta\mathbf{x} = \mathbf{x}_r - \mathbf{x}'_r$, and $\overline{\lambda}$ is the center wavelength between λ_l and λ'_l, and n is the refractive index of SRPM. Equation (8) reveals that the spectral resolution of GISC camera mainly depends on the parameter ω of SRPM, and the spatial resolution is still limited by Rayleigh's criterion [1] without considering the discernibility in the high-dimensional space.

In the viewpoint of matrix analysis, Eq. (1) is usually approximated as [16, 22]

$$\mathbf{y} = \mathbf{\Phi}\mathbf{X}, \tag{10}$$

in a way that the existing optimization theoretical achievements such as compressive sensing (CS) [23, 24]

can be directly applied, where $\mathbf{X} \in \mathbb{R}^n$ denotes the high-dimensional image of object, $\mathbf{y} \in \mathbb{R}^m$ is a reshaped intensity distributions $I_t(\mathbf{x}_t)$, the sampling matrix $\mathbf{\Phi} \in \mathbb{R}^{m\times n}$ whose columns consists of the speckle patterns $I_r(\mathbf{x}_t;\mathbf{x}_r,\lambda_l)$, m is the sample number. Considering sparsity priors, $\mathbf{X}$ in Eq. (10) can be retrieved by solving such an inverse problem

$$\min_{\mathbf{X}} \|\mathbf{X}\|_0 \ \text{ subject to } \quad \mathbf{y}-\bar{\mathbf{y}} = (\mathbf{\Phi}-\bar{\mathbf{\Phi}})\mathbf{X}, \tag{11}$$

where $\bar{\cdot}$ denotes an operation to calculate the mean value of column. For notational simplicity, we denote $\mathbf{\Psi} = \mathbf{\Phi}-\bar{\mathbf{\Phi}}$ and $\mathbf{y}_0 = \mathbf{y}-\bar{\mathbf{y}}$.

In the framework of CS, the mutual incoherence property (MIP) [23] is commonly used to analyze the inverse problem (11), which is defined as

$$\mu(\mathbf{\Psi}) = \max_{1\le i<j\le n} \frac{|\psi_i^T\psi_j|}{\|\psi_i\|_2\|\psi_j\|_2}, \tag{12}$$

where $\|\cdot\|_2$ is the ℓ_2-norm, and ψ_i denotes the i-th column of $\mathbf{\Psi}$.

The relationship between the normalized second-order correlation function $g^{(2)}(\mathbf{x}_r,\mathbf{x}_r';\lambda_l,\lambda_l')$ and MIP is

$$\begin{aligned}
\mu(\mathbf{\Psi}) &= \max_{1\le i<j\le n} \frac{|\psi_i^T\psi_j|}{\|\psi_i\|_2\|\psi_j\|_2} \\
&= \max_{1\le i<j\le n} \frac{\left|(\phi_i-\bar{\phi_i})^T(\phi_j-\bar{\phi_j})\right|}{\|\phi_i-\bar{\phi_i}\|_2\|\phi_j-\bar{\phi_j}\|_2} \\
&\overset{(a)}{\approx} \max_{1\le i<j\le n} \frac{\left|\phi_i^T\phi_j - m\langle\phi_i\rangle\langle\phi_j\rangle\right|}{\sqrt{mC(\phi_i)\langle\phi_i\rangle}\sqrt{mC(\phi_j)\langle\phi_j\rangle}} \\
&= \max_{1\le i<j\le n} \frac{1}{\sqrt{C(\phi_i)C(\phi_j)}}\left|\frac{\langle\phi_i\phi_j\rangle}{\langle\phi_i\rangle\langle\phi_j\rangle}-1\right| \\
&= \max_{1\le i<j\le n}\left|\frac{\langle\phi_i\phi_j\rangle}{\langle\phi_i\rangle\langle\phi_j\rangle}-1\right| = \max_{1\le i<j\le n}|g^{(2)}(i,j)|
\end{aligned} \tag{13}$$

where (a) is because the ensemble average of a random variable x is approximate to the mean value of its m measurements for a large m. The contrast $C(\phi_i)$ of speckle corresponding to the i-th column of $\mathbf{\Phi}$ is defined as $C(\phi_i) = (\phi_i-\langle\phi_i\rangle)^T(\phi_i-\langle\phi_i\rangle)/(m\langle\phi_i\rangle\langle\phi_i\rangle)$ and $C(\phi_i)=1$ in GI is because the probability of intensity of speckle obeys the negative exponential distribution.

Equation (13) indicates that $\mu(\mathbf{\Psi})$ is proportional to the maximum value of $g^{(2)}(i,j)$, which denotes the correlation of system responses of any two points in the high-dimensional space. That is, the MIP of a GISC camera represents the correlation of system responses of two nearest points in the high-dimensional space when the condition Eq. (14) is satisfied. Tropp [25] showed that $\mu < 1/(2K-1)$ is sufficient to guarantee the exact recovery of any K-sparse signals in the noiseless case by the orthogonal matching pursuit (OMP) algorithm and basis pursuit (BP) algorithm. Cai *et al.* [26] confirmed that this condition is sharp. Therefore, the nearest distance in the high-dimensional space to guarantee any K-sparse signals exactly recovery is bound by

$$\exp\left\{-\left(\frac{2\pi(n-1)\omega\Delta\lambda}{\bar{\lambda}^2}\right)^2\right\}\left(\frac{2J_1(\pi\frac{D\Delta\mathbf{x}}{\bar{\lambda}f_1})}{\pi\frac{D\Delta\mathbf{x}}{\bar{\lambda}f_1}}\right)^2 < \frac{1}{2K-1}. \tag{14}$$

Equation (14) builds the resolution bound of GISC camera in the high-dimensional space. Namely, we can guarantee the exactly recovery of K points when their differences $(\Delta\mathbf{x},\Delta\lambda)$ in the high-dimensional space exceed the constraint of Eq. (14). For a GISC camera, where $f_1 = 50$ mm, $f_2 = 300$ mm, $D = 1.48$ mm, $z_1 = 5$ mm, $z_2 = 40$ mm, $L = 200$ mm, $\omega = 3.5$ um, $\zeta = 12$ um and $\bar{\lambda} = 530$ nm, the Rayleigh's criterion of the objective lens is $\Delta\mathbf{x} = 1.22\lambda f_1/D \approx 21.8$ um, and the recovery resolution bound for $K=2$ in high-dimensional light field space is shown in Fig. 2. As observed in Fig. 2, the recovery spatial resolution is much better than Rayleigh's criterion. Moreover, the recovery spatial resolution is promoted by increasing the discernibility in spectral dimension.

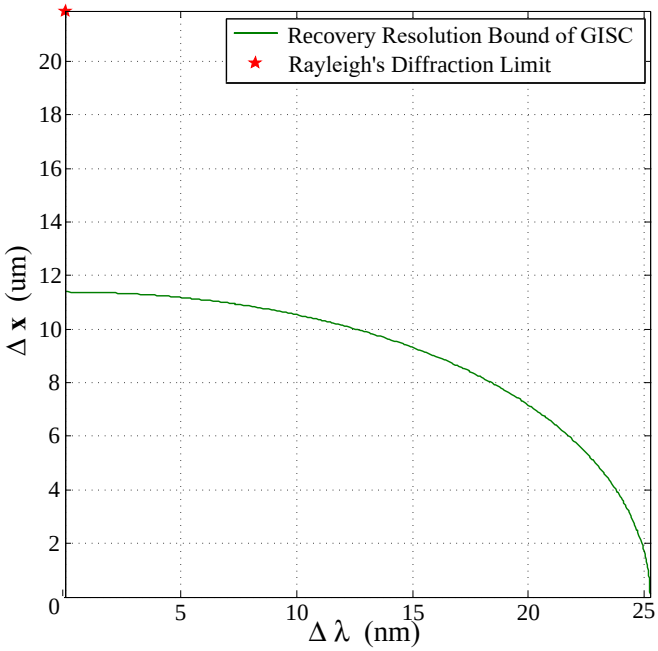

FIG. 2. Recovery resolution bound of GISC camera in high-dimensional light field space ($K=2$).

Fig. 3 represents the experimental system diagram of GISC camera. The focus length of the objective lens and the tube lens is $f_1 = 50$ mm and $f_2 = 300$ mm, respectively. The aperture diameter of the objective lens is $D = 1.48$ mm. A SRPM (DGUV10-1500, thorlab) is adopted in the experiments, and the corresponding diffraction limit is 21.8 um. A relay lens (UPlanSApo 4×, Olympus) is used to match the pixel size of CCD (Andor iKon-M, pixel size of 13 um) and the average size of the pre-determined speckle patterns. Moreover, as a comparison, a (1:9) beam splitter splits another optical path to record the blurred image by a detector (AVT camera Stingray F-504B). In the pre-determined calibration process, a monochrome light where a wide-band white source (Xenon lamp) is filtered by a monochrometer, is coupled into an optical fiber with core diameter 16 um. The experimental spectrum varies from 530 nm to 605 nm with spectral interval $\Delta\lambda_0 = 7.5$nm. When the opti-

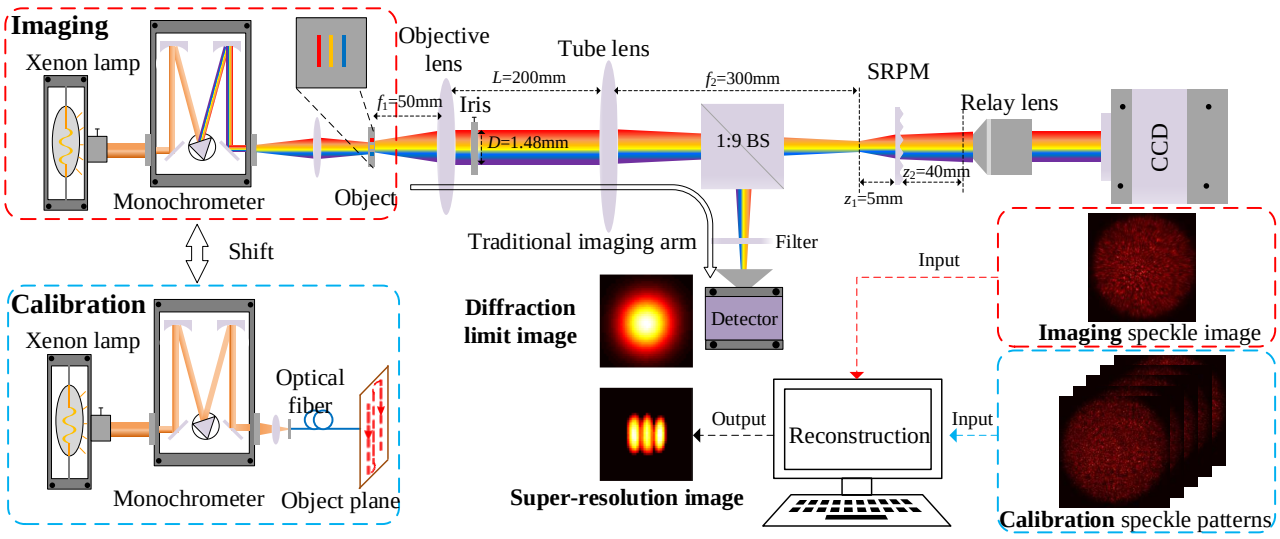

FIG. 3. Experimental system diagram of GISC camera.

cal fiber shifts $\Delta\mathbf{x} = 1$ um in the field of view 40 um $\times$ 40 um by an electric translation stage, the corresponding speckle patterns are recorded. In the imaging process, a multicolour object is placed on the object plane and the speckle images is obtained. By solving the problem (11), the spatial super-resolution image is reconstructed.

We construct a serials of objects which consists of two adjacent points with different spatial distance ($\Delta\mathbf{x} = 3$ um, 5 um, $\cdots$, 29 um) and spectral difference $\Delta\lambda = 0$ nm, 7.5 nm and 15 nm. $\mathbf{y}$ is produced by Eq. (10), where an experimental sampling matrix $\mathbf{\Phi}$ is obtained in the pre-determined calibration process. For each distance ($\Delta\mathbf{x}$,$\Delta\lambda$), we perform 100 independent trials by changing the absolute positions of two point sources. In each trial, we adopt OMP algorithm to recover the image and use the testing strategy in [27] by checking the empirical frequency of exact reconstruction of two adjacent points (shown in Fig. 4(a)). On the point of statistical resolution, the localization precision represents the performance of GISC camera's resolution [28–30]. By calculating the Euclidean distance between reconstructed points and real points, we use the localization error to measure the distribution of the reconstructed point around the real point in Fig. 4(b). The diffraction limit of GISC camera is 21.8 um. The recovery resolution bound ($K = 2$) for $\Delta\lambda = 0$ nm, 7.5 nm and 15 nm are 11.38 um, 10.92 um, 9.32 um, respectively. Since the calibrated point light source for each wavelength in the experiment is not an ideal monochrome light and the dispersion of light through spatial light modulator decrease the calibration speckles contract, $g^{(2)}(\mathbf{x}_r, \mathbf{x}'_r; \lambda_l, \lambda'_l)$ of the experimental sampling matrix $\mathbf{\Phi}$ is 0.3, which is less than 1. It leads to the recovery performance of GISC camera as a function of the distance in the high-dimensional space doesn't reach the recovery resolution bound in Fig. 2. As shown in Fig. 4, the spectral difference of two point sources is conducive to promote the frequency of the exactly recovery as well as the location accuracy. The simulation results in Fig. 2 and Fig 4 indicate that the discernibility in high-dimension light field space (such as spectral dimension) indeed improves the spatial resolution of GISC camera and achieves breaking Rayleighs criterion in spatial domain.

Two adjacent points at different spatial separation distances $\Delta\mathbf{x}$ and wavelength intervals $\Delta\lambda$ is selected for experimental resolution analysis. As shown in Fig. 5(a), we choose three different spatial separation distances 4 um, 4.57 um and 5.14 um, and the corresponding wavelength intervals are 23 nm, 17 nm and 9 nm, respectively. The diffraction limited images and reconstructed super-resolution images are shown in Fig. 5(b) and (c). Fig. 5(d) draws the relationship between the spatial resolution of GISC camera and the wavelength interval $\Delta\lambda$ of object, which implies that the spatial resolution of GISC camera is improved by increasing the spectral difference.

Fig. 6 represents the experimental result of three slits. As shown in Fig. 6(a) and (b), its spatial seperation distance and wavelength interval are 5 um and 15 nm, respectively. Fig. 6(c) and (d) show the corresponding diffraction limited image and the reconstructed super-resolution image. Since the diffraction limit is 21.8 um and three slits' spatial seperation distance is 5 um, it implies that based on the discernibility in the $(\mathbf{x}, \lambda)$ dimensional light field space, over four folds of Rayleigh's criterion is achieved in this experiment.

The discernibility in the polarization dimensional space is also investigated. Two adjacent points with different linear polarization states are selected as an object. The distance between two points is 4 um, 6 um, 8 um and 10 um, respectively. By rotating a polarizer to different detections of polarization θ (0°, 45°, 90°, and 135°) in front of CCD, a polarized detector is built. Fig. 7 shows

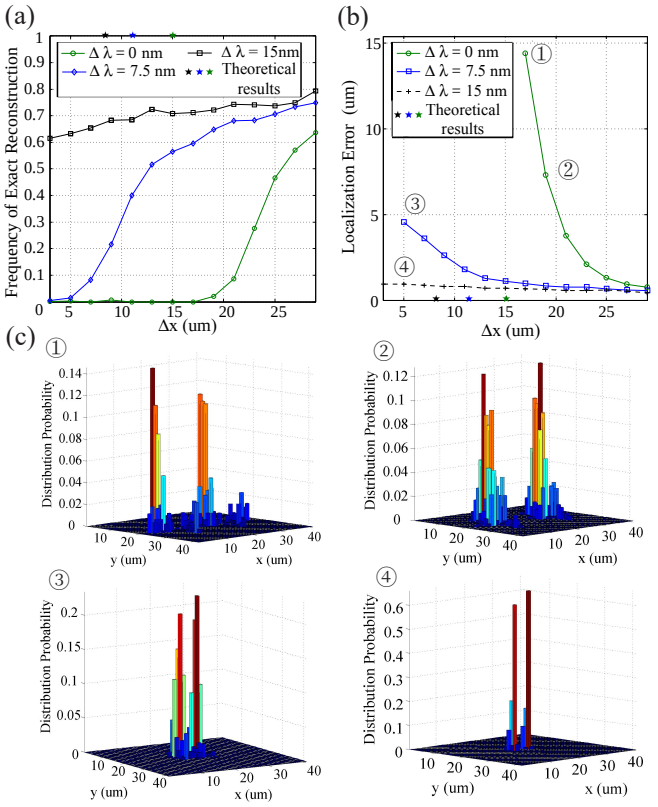

FIG. 4. The recovery performance of GISC camera as a function of the distance in the high-dimensional space. (a) Frequency of exact recovery as a function of the distance of two points in high-dimensional light field space ($\Delta\mathbf{x}$, $\Delta\lambda$). (b) The localization error as a function of the distance of two points in high-dimensional light field space ($\Delta\mathbf{x}$, $\Delta\lambda$). (c) The distribution probability of localizations in (b). The diffraction limit of GISC camera is 21.8 um. The recovery resolution bound ($K = 2$) for $\Delta\lambda = 0$ nm, 7.5 nm and 15 nm are 11.38 um, 10.92 um, 9.32 um, respectively.

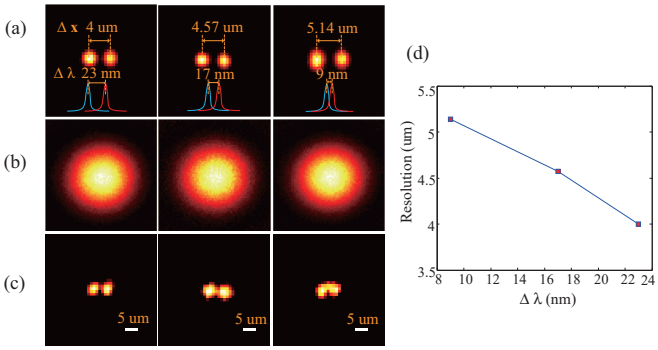

FIG. 5. Experimental results of two points. (a) The object consists of two adjacent points at different spatial separation distances $\Delta\mathbf{x}$ and wavelength intervals $\Delta\lambda$. (b) The diffraction limited images of object. (c) The reconstructed images. (d) The spatial resolution as a function of the wavelength interval $\Delta\lambda$.

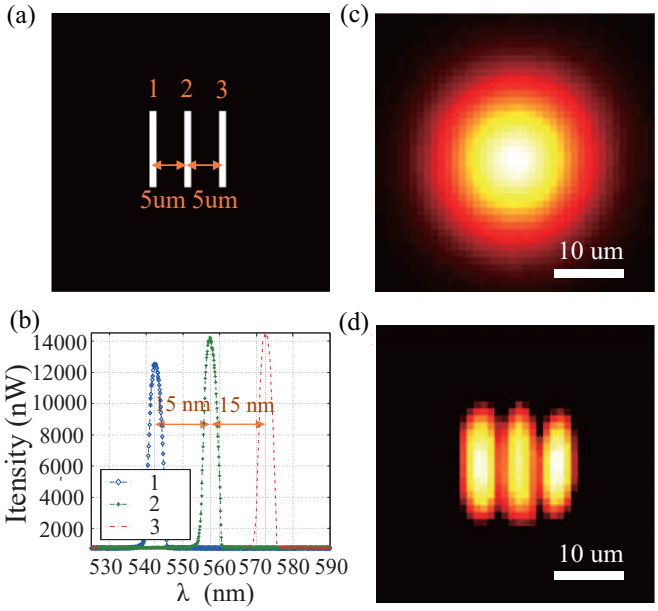

FIG. 6. Experimental results of three slits. (a) The object consists of three slits, the spatial interval between each slit is 5 um. (b) The spectral distribution of each slit, where the wavelength interval between each slit is 15 nm. (c) The diffraction limited image of object. (d) The reconstructed image.

the spatial resolution as a function of the polarization state's difference $\Delta\theta$. Based on the difference of the polarization state, the best spatial resolution is 4 um, which is five folds of Rayleigh's criterion. It observes that the spatial resolution is also promoted by increasing the difference of the polarization state.

In this paper we demonstrate both theoretically and experimentally that, on the contrary to eliminate the propagation effects relative to wavelength and polarization in conventional camera, the non-spatial dimensional discrepant information of light field irradiated from object can be exploited to break spatial Rayleighs criterion of GISC camera. There is still Rayleighs curse induced by diffraction effect when resolving two closely-spaced points in high-dimensional light field space. However, considering the spatial resolution of two closed-located points, the Rayleighs curse can be avoided only if two points are distinguishable on other dimensions of light field. Therefore the spatial resolution beyond the Rayleigh limit is indeed possible based on the discernibility in the high-dimensional space.

Some next work are as follows. 1) As a computational imaging technology, the super-resolution ability of GISC camera strongly depends on the recovery algorithm, and the current computational complexity for the large sensing matrix is prohibitively high. Therefore, there is a large space to improve for developing new high-efficiency recovery algorithms that can integrate more prior information [31, 32], new method of precondition the sensing matrix [33] and new recovery approach to reduce the computational complexity [34, 35]. 2) The super-resolution ability can be further enhanced by optimizing

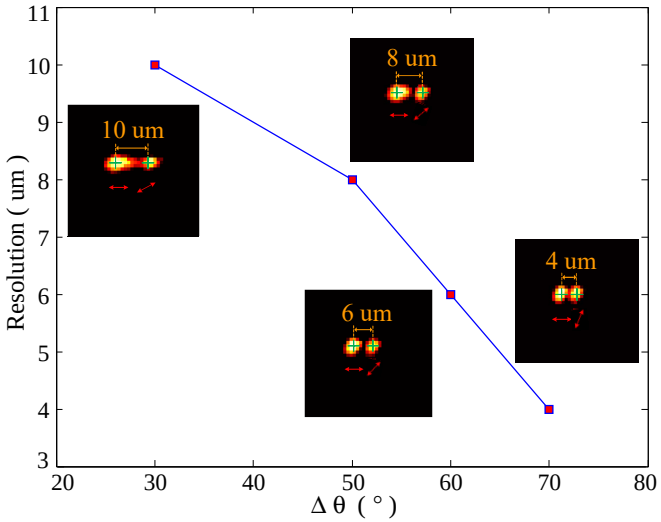

FIG. 7. Spatial resolution as a function of the polarization state's difference $\Delta\theta$.

the random phase modulator and detection for higher imaging efficiency [36] and signal-to-noise ratio (SNR) [37, 38]. 3) Appealing directly to concepts in information theory, research forward in an overall methodology of studying imaging system and follow-up processing is extremely important for the confidence level of GI. Different from the canonical case study of resolving two closely-spaced sources with possibly unequal brightness to investigate the performance of conventional incoherent imaging systems and image restoration techniques in the point-to-point imaging scenario [10], the overall performance of GI systems strongly depends on the structure of the signal to be restored, and the constraints based on prior information should be included in analysis tools from modern statistical detection and estimation theory [39, 40]. And 4) Considering more practical factors of imaging, the theoretical work of the condition in Eq. (14) needs further study.

High-dimensional light field contains rich information about the natural or artificial scenes, which widely exists in astronomy [41], fluorescence microscopy [42], stimulated Raman scattering microscopy [43] and polarization microscopy [44]. Recently GISC nanoscopy with 80 nm spatial resolution in a single frame has been experimentally demonstrated by utilizing only the sparsity of fluorescence emitters [29]. As demonstrated in this paper, GISC nanoscopy exploiting the discernibility of light field in the high-dimensional space will further promote its performance in breaking the classical Rayleigh limit of spatial resolution. Compared to existing physical super-resolution methods, the technology of breaking Rayleighs criterion based on the discernibility in high-dimensional light field space, which is in consistent with CS, has higher information acquisition efficiency, and can achieve wide-field super-resolution imaging in a singleshot. Therefore, it can not only be directly applied to remote sensing, but also can be applied to the wide-field super-resolution detection of dynamic processes with the detection sensitivity and SNR guaranteed. With the rapid development in signal processing [45–47], light field modulation (such as metasurface [28, 48, 49]), and detection [50] technologies, it will be widely applied in remote sensing, microscopy and astronomy.

This work is supported in part by National Key Research and Development Program of China (2017YFB0503303) and National Natural Science Foundation of China (61971146).

*These authors contributed equally to this work.

†Corresponding author: sshan@mail.shcnc.ac.cn

[1] M. Born, E. Wolf, Principles of optics: electromagnetic theory of propagation, interference and diffraction of light., no. 465–467, Cambridge University Press (CUP), 1999.

[2] R. Heintzmann, M. G. Gustafsson, Subdiffraction resolution in continuous samples, Nature Photonics 3 (7) (2009) 362–364.

[3] C. Sheppard, T. Wilson, The theory of the direct-view confocal microscope, Journal of microscopy 124 (2) (1981) 107–117.

[4] U. Dürig, D. W. Pohl, F. Rohner, Near-field optical-scanning microscopy, Journal of applied physics 59 (10) (1986) 3318–3327.

[5] S. W. Hell, J. Wichmann, Breaking the diffraction resolution limit by stimulated emission: stimulated-emission-depletion fluorescence microscopy, Optics letters 19 (11) (1994) 780–782.

[6] M. J. Rust, M. Bates, X. Zhuang, Sub-diffraction-limit imaging by stochastic optical reconstruction microscopy (storm), Nature methods 3 (10) (2006) 793–796.

[7] E. Betzig, G. H. Patterson, R. Sougrat, O. W. Lindwasser, S. Olenych, J. S. Bonifacino, M. W. Davidson, J. Lippincott-Schwartz, H. F. Hess, Imaging intracellular fluorescent proteins at nanometer resolution, Science 313 (5793) (2006) 1642–1645.

[8] C. Helstrom, Quantum detection and estimation theory, academic press, New York (1976).

[9] M. Tsang, R. Nair, X.-M. Lu, Quantum theory of superresolution for two incoherent optical point sources, Physical Review X 6 (3) (2016) 031033.

[10] M. Tsang, Conservative classical and quantum resolution limits for incoherent imaging, Journal of Modern Optics 65 (11) (2018) 1385–1391.

[11] S. Chaudhuri (Ed.), Super-Resolution Imaging, Kluwer Academic Publishers, 2002.

[12] A. Papoulis, A new algorithm in spectral analysis and band-limited extrapolation, IEEE Transactions on Circuits and systems 22 (9) (1975) 735–742.

[13] S. C. Park, M. K. Park, M. G. Kang, Super-resolution image reconstruction: a technical overview, IEEE signal processing magazine 20 (3) (2003) 21–36.

[14] C. Dong, C. C. Loy, K. He, X. Tang, Image super-resolution using deep convolutional networks, IEEE

transactions on pattern analysis and machine intelligence 38 (2) (2015) 295–307.
[15] E. H. Adelson, J. R. Bergen, et al., The plenoptic function and the elements of early vision, Vol. 2, Vision and Modeling Group, Media Laboratory, Massachusetts Institute of Technology, 1991.
[16] S. Han, H. Yu, X. Shen, H. Liu, W. Gong, Z. Liu, A review of ghost imaging via sparsity constraints, Applied Sciences 8 (8) (2018) 1379.
[17] Z. Liu, S. Tan, J. Wu, E. Li, X. Shen, S. Han, Spectral camera based on ghost imaging via sparsity constraints, Scientific reports 6 (2016) 25718.
[18] Y. Bromberg, O. Katz, Y. Silberberg, Ghost imaging with a single detector, Physical Review A 79 (5) (2009) 053840.
[19] J. W. Goodman, Statistical optics, no. 33–41, John Wiley & Sons, 2015.
[20] I. Reed, On a moment theorem for complex gaussian processes, IRE Transactions on Information Theory 8 (3) (1962) 194–195.
[21] S. K. Sinha, E. B. Sirota, S. Garoff, H. B. Stanley, X-ray and neutron scattering from rough surfaces, Physical Review B 38 (4) (1988) 2297–2311.
[22] O. Katz, Y. Bromberg, Y. Silberberg, Compressive ghost imaging, Applied Physics Letters 95 (13) (2009) 131110.
[23] D. L. Donoho, X. Huo, Uncertainty principles and ideal atomic decomposition, IEEE transactions on information theory 47 (7) (2001) 2845–2862.
[24] E. J. Candes, T. Tao, Decoding by linear programming, IEEE transactions on information theory 51 (12) (2005) 4203–4215.
[25] J. A. Tropp, Greed is good: Algorithmic results for sparse approximation, IEEE Transactions on Information theory 50 (10) (2004) 2231–2242.
[26] T. T. Cai, L. Wang, G. Xu, Stable recovery of sparse signals and an oracle inequality, IEEE Transactions on Information Theory 56 (7) (2010) 3516–3522.
[27] W. Dai, O. Milenkovic, Subspace pursuit for compressive sensing signal reconstruction, IEEE transactions on Information Theory 55 (5) (2009) 2230–2249.
[28] F. Aieta, M. A. Kats, P. Genevet, F. Capasso, Multiwavelength achromatic metasurfaces by dispersive phase compensation, Science 347 (6228) (2015) 1342–1345.
[29] W. Li, Z. Tong, K. Xiao, Z. Liu, Q. Gao, J. Sun, S. Liu, S. Han, Z. Wang, Single-frame wide-field nanoscopy based on ghost imaging via sparsity constraints, Optica 6 (12) (2019) 1515–1523.
[30] M. Shahram, P. Milanfar, Statistical and information-theoretic analysis of resolution in imaging, IEEE Transactions on Information Theory 52 (8) (2006) 3411–3437.
[31] J. Scarlett, J. S. Evans, S. Dey, Compressed sensing with prior information: Information-theoretic limits and practical decoders, IEEE Transactions on Signal Processing 61 (2) (2013) 427–439.
[32] X. Zhang, W. Cui, Y. Liu, Compressed sensing with prior information via maximizing correlation, in: 2017 IEEE International Symposium on Information Theory (ISIT), IEEE, 2017.
[33] Z. Tong, J. Wang, S. Han, Preconditioned multiple orthogonal least squares and applications in ghost imaging via sparsity constraint, arXiv preprint arXiv:1910.04926 (2019).
[34] H. Palangi, R. Ward, L. Deng, Distributed compressive sensing: A deep learning approach, IEEE Transactions on Signal Processing 64 (17) (2016) 4504–4518.
[35] R. Zhu, H. Yu, Z. Tan, R. Lu, S. Han, Z. Huang, J. Wang, Ghost imaging based on y-net: a dynamic coding and conjugate-decoding approach, arXiv preprint arXiv:2002.03824 (2020).
[36] C. Hu, Z. Tong, Z. Liu, Z. Huang, J. Wang, S. Han, Optimization of light fields in ghost imaging using dictionary learning, Optics Express 27 (20) (2019) 28734.
[37] S. Liu, Z. Liu, C. Hu, E. Li, X. Shen, S. Han, Spectral ghost imaging camera with super-rayleigh modulator, arXiv preprint arXiv:1910.04461 (2019).
[38] D. Yang, G. Wu, B. Luo, L. Yin, Ghost imaging with the optimal binary sampling, ResearchGet (2020).
[39] E. Nitzan, T. Routtenberg, J. Tabrikian, Limitations of constrained CRB and an alternative bound, in: 2018 IEEE Statistical Signal Processing Workshop (SSP), IEEE, 2018.
[40] A. Echeverria, J. F. Silva, R. A. Mendez, M. Orchard, Analysis of the bayesian cramér-rao lower bound in astrometry, Astronomy & Astrophysics 594 (2016) A111. doi:10.1051/0004-6361/201628220.
[41] B. A. Wilking, M. J. Lebofsky, J. C. Kemp, P. G. Martin, G. H. Rieke, The wavelength dependence of interstellar linear polarization, The Astrophysical Journal 235 (1980) 905. doi:10.1086/157694.
[42] N. Ji, Adaptive optical fluorescence microscopy, Nature Methods 14 (4) (2017) 374–380. doi:10.1038/nmeth.4218.
[43] M. Ji, S. Lewis, S. Camelo-Piragua, S. H. Ramkissoon, M. Snuderl, S. Venneti, A. Fisher-Hubbard, M. Garrard, D. Fu, A. C. Wang, J. A. Heth, C. O. Maher, N. Sanai, T. D. Johnson, C. W. Freudiger, O. Sagher, X. S. Xie, D. A. Orringer, Detection of human brain tumor infiltration with quantitative stimulated raman scattering microscopy, Science Translational Medicine 7 (309) (2015) 309ra163–309ra163. doi:10.1126/scitranslmed.aab0195.
[44] K. Zhanghao, J. Gao, D. Jin, X. Zhang, P. Xi, Super-resolution fluorescence polarization microscopy, Journal of Innovative Optical Health Sciences 11 (01) (2017) 1730002. doi:10.1142/s1793545817300026.
[45] E. C. Marques, N. Maciel, L. Naviner, H. Cai, J. Yang, A review of sparse recovery algorithms, IEEE Access 7 (2019) 1300–1322.
[46] H. Yao, F. Dai, S. Zhang, Y. Zhang, Q. Tian, C. Xu, DR2-net: Deep residual reconstruction network for image compressive sensing, Neurocomputing 359 (2019) 483–493.
[47] S.-W. Hu, G.-X. Lin, S.-H. Hsieh, C.-S. Lu, Performance analysis of joint-sparse recovery from multiple measurement vectors via convex optimization: Which prior information is better?, IEEE Access 6 (2018) 3739–3754.
[48] H. Kwon, E. Arbabi, S. M. Kamali, M. Faraji-Dana, A. Faraon, Computational complex optical field imaging using a designed metasurface diffuser, Optica 5 (8) (2018) 924.
[49] S. Colburn, A. Zhan, A. Majumdar, Metasurface optics for full-color computational imaging, Science Advances 4 (2) (2018) eaar2114.
[50] C. Inc., Canon develops aps-h-size cmos sensor with approximately 250 megapixels, the world's highest pixel count for its size, https://global.canon/en/news/2015/sep07e.html.